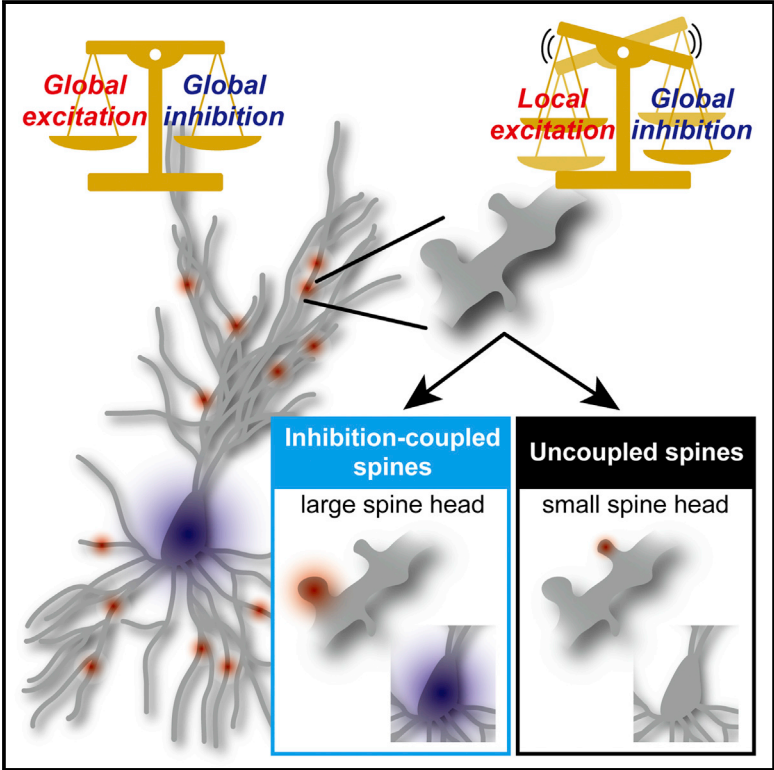


## Subcellular Imbalances in Synaptic Activity

### Graphical Abstract



### Authors

Naoya Takahashi, Chiaki Kobayashi, Tomoe Ishikawa, Yuji Ikegaya

### Correspondence

yuji@ikegaya.jp

### In Brief

Takahashi et al. find that, although global GABAergic inhibition counterbalances synaptic excitation on dendritic trees, this balance breaks down at the microscopic level since only large synapses are excited by this inhibition.

### Highlights

- Excitation and inhibition are instantaneously balanced within a neuron
- This balance is disrupted at dendritic segment lengths of less than 50 μm
- The activity of only 22% of the spines is accompanied by somatic inhibition
- The inhibition-coupled activity tends to occur in large spine heads

# Subcellular Imbalances in Synaptic Activity

Naoya Takahashi,<sup>1,3</sup> Chiaki Kobayashi,<sup>1</sup> Tomoe Ishikawa,<sup>1</sup> and Yuji Ikegaya<sup>1,2,\*</sup>

<sup>1</sup>Laboratory of Chemical Pharmacology, Graduate School of Pharmaceutical Sciences, The University of Tokyo, Bunkyo-ku, Tokyo 113-0033, Japan

<sup>2</sup>Center for Information and Neural Networks, National Institute of Information and Communications Technology, Suita City, Osaka 565-0871, Japan

<sup>3</sup>Present address: Charité Universitätsmedizin Berlin, Neuroscience Research Center, Charitéplatz 1, 10117 Berlin, Germany

\*Correspondence: [yuji@ikegaya.jp](mailto:yuji@ikegaya.jp)

<http://dx.doi.org/10.1016/j.celrep.2016.01.024>

This is an open access article under the CC BY license (<http://creativecommons.org/licenses/by/4.0/>).

## SUMMARY

The dynamic interactions between synaptic excitation and inhibition (E/I) shape membrane potential fluctuations and determine patterns of neuronal outputs; however, the spatiotemporal organization of these interactions within a single cell is poorly understood. Here, we investigated the relationship between local synaptic excitation and global inhibition in hippocampal pyramidal neurons using functional dendrite imaging in combination with whole-cell recordings of inhibitory postsynaptic currents. We found that the sums of spine inputs over dendritic trees were counterbalanced by a proportional amount of somatic inhibitory inputs. This online E/I correlation was maintained in dendritic segments that were longer than 50  $\mu\text{m}$ . However, at the single spine level, only 22% of the active spines were activated with inhibitory inputs. This inhibition-coupled activity occurred mainly in the spines with large heads. These results shed light on a microscopic E/I-balancing mechanism that operates at selected synapses and that may increase the accuracy of neural information.

## INTRODUCTION

The synaptic interplay between excitation and inhibition (E/I) is fundamental to cortical circuit operation (Froemke, 2015; Isaacson and Scanziani, 2011), and its roles in both spontaneous activity and sensory processing have been demonstrated in many cortical regions (Anderson et al., 2000; Okun and Lampl, 2008; Wehr and Zador, 2003). To investigate the correlation between E/I in spontaneous or evoked synaptic responses, previous studies have recorded E/I separately in respective trials because simultaneously recording E/I from a single cell is technically demanding. To overcome this difficulty, some studies have recorded ongoing excitatory and inhibitory inputs from two adjacent neurons (Okun and Lampl, 2008) or recorded them nearly simultaneously from a single neuron by rapidly alternating the holding membrane voltages (Cafaro and Rieke, 2010). Thus, esti-

imating the instantaneous E/I balance in individual neurons remains challenging. In addition, the E/I balance is almost undescribed at a subcellular resolution (Liu, 2004). In the present study, we recorded excitatory inputs using a functional calcium imaging technique that probes the activity of spines at a single synapse resolution (Chen et al., 2011; Chen et al., 2013; Takahashi et al., 2012; Yuste and Denk, 1995), while we recorded inhibitory postsynaptic currents (IPSCs) from the same neurons using the whole-cell voltage-clamp technique. We then investigated the temporal and spatial relationships between the subcellular excitatory inputs and the somatic inhibitory inputs.

## RESULTS

### Simultaneous Recording of Excitatory and Inhibitory Inputs from a Single Cell

We loaded CA3 pyramidal cells contained in organotypic hippocampal slices with the fluorescent calcium indicator Fluo-5F using somatic patch-clamp pipettes and optically recorded the spontaneous calcium events in spines at 20 Hz using a Nipkow disk-based confocal microscope (Figure 1A) (Takahashi et al., 2012). In total, 918 spines were identified in 12 videos from ten cells. Each video contained  $77 \pm 23$  spines (mean  $\pm$  SD, ranging from 45 to 118 spines) in a microscopic field of approximately  $100 \times 100 \mu\text{m}^2$ . Of the 918 spines, 581 (63.3%) were spontaneously active, emitting calcium activity at frequencies of  $0.028 \pm 0.054$  Hz (ranging from 0.003 to 0.68 Hz). We previously reported that these calcium transients were abolished by NMDA receptor antagonists (Takahashi et al., 2012). Moreover, the number of spines activated in each video frame, termed herein summed spine activity, was positively correlated with the time integral (charge transfer) of the excitatory postsynaptic currents (EPSCs) that were simultaneously recorded from the soma (Figure S1; Pearson's  $r = 0.44$ ,  $p = 1.4 \times 10^{-3}$ , and  $n = 46,787$  frames in 13 videos). We thus conclude that the calcium transients in spines reflect excitatory synaptic inputs. The times of synaptic inputs were individually determined based on the onset times for calcium events in spines (Figure 1B, top), and the total number of synaptic inputs was counted in each video frame to estimate the level of ongoing synaptic excitation in the imaged regions.

To reliably capture NMDA receptor-dependent calcium events, we clamped the patched neurons continuously at  $-30$  mV

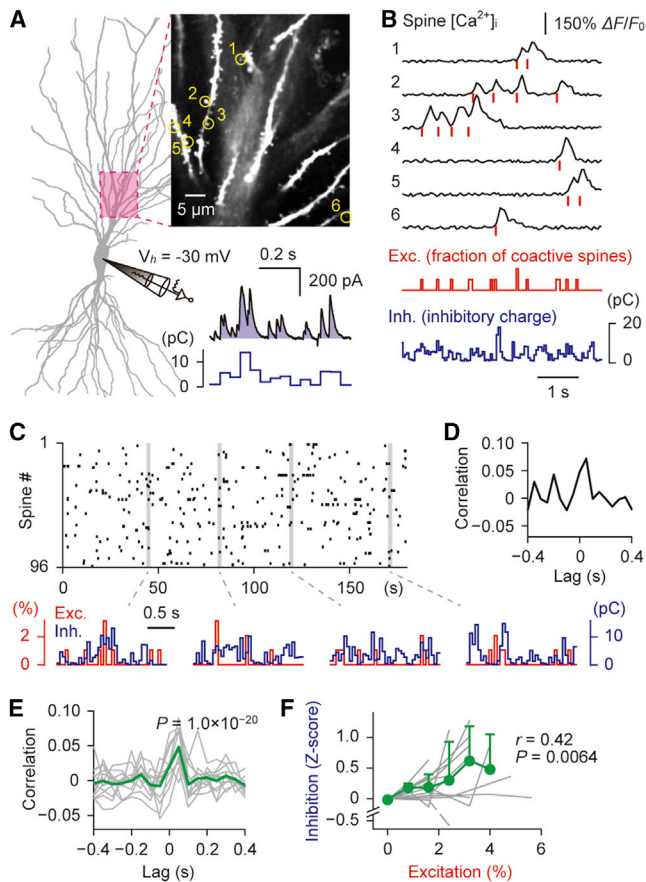


**Figure 1. Globally Balanced E/I in Dendritic Trees**

(A) Spine activity was imaged using confocal microscopy in the dendrites (top right) of a CA3 pyramidal cell (left), and IPSCs were whole-cell recorded from the soma (bottom right). The inhibitory charge transfer (blue line) was calculated from the IPSCs every 50 ms (= 1 video frame).

(B) The top traces indicate the spontaneous calcium activity in the six representative spines numbered in (A). Each red vertical line shows the onset time for the activity. The middle red histogram indicates the time course for the number of co-activated spines, whereas the bottom blue histogram indicates the inhibitory charge transfers that were simultaneously recorded from the soma.

(C) The raster plot shows the spatiotemporal patterns of calcium activity in 96 spines in the imaged dendritic branches that are shown in (A). The four bottom insets indicate time-expanded examples of the synaptic E/I levels.

(D) A cross-correlogram is shown to describe the summed spine activity and the inhibitory charge transfers in the cell in (C), indicating that inhibition followed excitation.

(E) E/I cross-correlograms of 12 videos (gray lines) were averaged (green), resulting in a significant peak at 50 ms ( $p = 1.0 \times 10^{-20}$ ,  $Z = 9.34$ , Z-test, and  $n = 12$  videos).

(F) Relationship between the summed spine activity in a given video frame and inhibitory charge transfers. The green line represents the mean  $\pm$  SD of 12 videos (gray lines). The E/I were significantly balanced (Pearson's  $r = 0.42$ ,  $p = 6.4 \times 10^{-3}$ ).

(Takahashi et al., 2012). This voltage is close to the reversal potential of excitatory inputs. Thus, we primarily recorded outward synaptic currents, i.e., IPSCs, but a small fraction of inward currents, i.e., EPSCs, remained. This feature allowed us to discriminate

IPSCs from EPSCs based on the directions of their waveforms. Incidentally, we measured the amount of phasic excitatory and inhibitory currents at holding voltages of  $-70$  mV and  $0$  mV (corresponding to the reversal potentials for IPSCs and EPSCs, respectively). The ratio of inhibitory to excitatory conductances was estimated to be  $5.2 \pm 1.9$  under our experimental conditions; that is, IPSCs contributed  $86.2\% \pm 5.1\%$  of the total PSCs that were recorded at  $-30$  mV (Figure S2; mean  $\pm$  SD and  $n = 5$  cells). Therefore, contamination with EPSCs, if any, was minimal in the outward PSCs we measured here. We then calculated the time integral for IPSCs every 50 ms to measure inhibitory charge transfer (Figure 1A, bottom). This bin size was equal to the length of a single video frame, which allowed us to directly compare the time course of somatic IPSCs to the time course of the summed spine activity (Figure 1B, bottom). Thus, we were able to compare subcellular excitation and global inhibition within a single neuron.

### E/I Balance Is Maintained over Dendritic Trees

A representative comparison of E/I is shown in Figure 1C. This video contained 96 spines. The cross-correlogram between summed spine activity and inhibitory charge transfers exhibited a peak at an offset of 50 ms, i.e., one video frame (Figure 1D), demonstrating that spine excitation was followed by somatic inhibition, with a short delay between the two. The same analyses for all 12 videos revealed a peak offset of approximately 0–50 ms, suggesting an overall consistency in excitation-to-inhibition sequences (Figure 1E). The mean peak value of the E/I correlations was as low as 0.052, but it was significantly higher than the baseline ( $p = 1.0 \times 10^{-20}$ ,  $Z = 9.34$ , Z-test, and  $n = 12$  videos). When we separately analyzed individual videos, 9 of the 12 videos exhibited significant peaks in the cross-correlograms. Thus, subcellular synaptic excitation generally occurred with global inhibition.

We next evaluated the E/I balance at every moment. For each video frame, we plotted the summed spine activity against the inhibitory charge transfer observed between 0 and 100 ms after that frame. We found that the inhibition level was positively correlated with the summed spine activity (Figure 1F; Pearson's  $r = 0.42$ ,  $p = 6.4 \times 10^{-3}$ , and  $n = 44,400$  frames in 12 videos). A Jonckheere-Terpstra trend test also confirmed that inhibition increased as a function of the summed spine activity ( $p = 4.9 \times 10^{-15}$ ,  $Z = 3.47$ ). Thus, dendritic activation was counteracted by a proportional amount of global inhibition; that is, subcellular synaptic excitation was balanced by global inhibition.

### Destabilized E/I Balance at Local Dendritic Domains

Next, we examined whether synaptic excitation at single branches is balanced by global inhibition. From 12 videos, we isolated 28 stretches of branches that contained more than ten spines, but no branching points. We plotted cross-correlograms between the summed spine activity and inhibitory charge transfers for individual branches (Figure 2A). Longer dendritic stretches tended to exhibit larger peaks in their cross-correlograms (Figure 2B;  $p = 0.052$  and Jonckheere-Terpstra trend test). The peak amplitudes were significant in 11 out of 28 branches (Figure 2B, purple circles). To illustrate the variability in E/I balance in local synaptic excitability, we calculated the

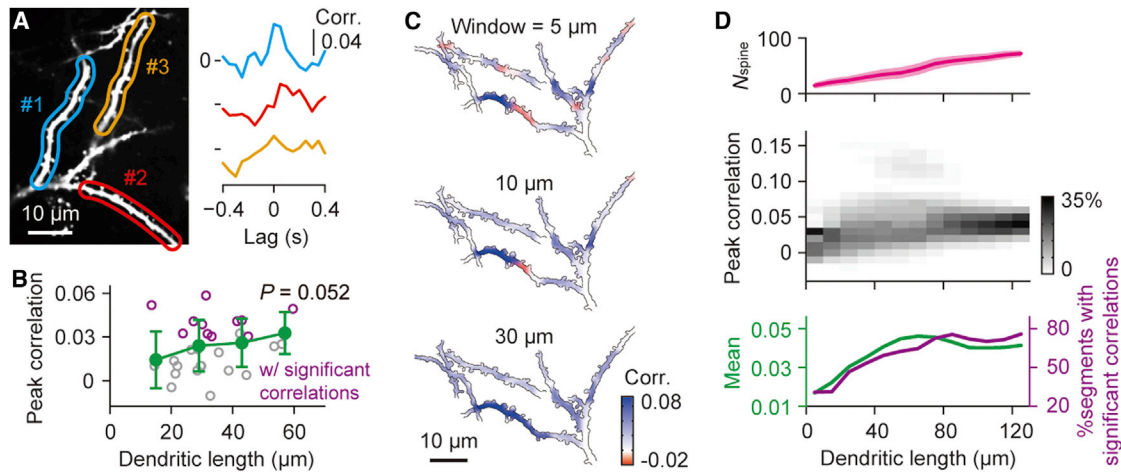


**Figure 2. E/I Balance in Local Dendritic Segments**

(A) Dendritic trees imaged in a confocal plane were separated into three branches (as shown at left, #1–3). Their E/I cross-correlograms exhibited peaks with a time offset of <100 ms (right).  
 (B) E/I correlations in single dendritic branches. Data from individual branches (open circles) are plotted with their means  $\pm$  SDs (green circles). The branches that exhibited significant correlation peaks are shown in purple. The peak correlation tended to be larger in longer dendritic branches ( $p = 0.052$  and Jonckheere-Terpstra trend test).  
 (C) Map of E/I correlations over the dendritic trees shown in (A). Local E/I correlations were calculated by sliding a window with various lengths (5, 10, or 30  $\mu\text{m}$ ) every 2  $\mu\text{m}$  along the dendrites, and the correlation peak values were plotted using a pseudo-colored scale.  
 (D) E/I correlations as a function of the lengths of the dendritic segments. The “virtual dendrites” were generated using different sets of dendritic parts from a single cell ( $n = 6,144$  segments). The numbers of spines that were involved in the summed segments increased linearly with their length (mean  $\pm$  SD, pink). The middle gray-scale map shows the distribution of the peak values of the E/I correlations. Their mean values are summarized as the green line shown in the bottom plot. The ratio of dendritic segments with significant correlation peaks to the total number of segments tested is shown as a purple line.

E/I correlations for summed spine activity within individual dendritic segments with various lengths and mapped the correlations onto the dendritic trees (Figure 2C). The map demonstrated that the E/I correlations were locally heterogeneous.

To investigate the relationship between E/I balance and dendritic length, we generated pseudo-stretches of dendrites with various lengths. The dendrites were randomly partitioned into smaller segments so that each segment contained 4–7 spines. Within each cell, 1–28 segments were arbitrarily combined to produce different sums of dendritic lengths. We created a total of 6,144 combinations using a random number generator and plotted their E/I correlation peaks as a function of the summed dendritic lengths (Figure 2D, middle and bottom). Note that in this analysis, we mixed segments from different dendritic branches within a cell because as a whole, the E/I correlations did not differ between the segments collected from the same dendritic branches and those collected from different branches (Figure S3A). The mean E/I correlations dropped suddenly at approximately <50  $\mu\text{m}$  (Figure 2D, bottom, green). In the same plot, we superimposed the ratio of the segments that exhibited significant peaks (Figure 2D, bottom, purple). This ratio also decreased at <50  $\mu\text{m}$ . These results suggest that the microscopic E/I balance collapsed at <50  $\mu\text{m}$ . A similar “critical” length was not observed when we conducted the same analysis for the transfer charges of EPSCs. We found that the correlations in that analysis gradually decreased for shorter dendritic segments, but were still largely significant even in 10- $\mu\text{m}$  dendritic segments (Figure S3B).

### Counteracting Inhibition in a Select Small Number of Spines

The E/I balance was collapsed in small dendritic domains, but on average, a 50- $\mu\text{m}$ -long segment still contained  $34.3 \pm 9.5$  imaged spines (Figure 2D, top). We therefore examined the E/I balance at the single synapse level. We plotted histograms for the peri-activity time of IPSCs (Figure 3A) in which inhibitory charge transfers were time-aligned to the onsets of the calcium events in each spine and averaged across all of the events. In some of the spines, this activity was accompanied by a transient increase in somatic inhibition, whereas other spines exhibited activity without apparent changes in somatic inhibition (Figure 3B). We estimated the statistical confidence levels for inhibition using a bootstrap resampling method (Figure S4A). To reduce false-positive errors, we analyzed 175 active spines that exhibited more than four calcium transients during the observation period. The distribution of the bootstrap-estimated Z-values was tailed toward higher values ( $p = 1.3 \times 10^{-3}$ , Shapiro-Wilk test, and Pearson’s moment coefficient of skewness = 0.66) and exhibited distributions with two peaks of  $Z \approx 0.5$  and  $Z \approx 3.5$  (Figure S4B). These peaks were observed regardless of the threshold used for the number of calcium transients, which varied between three and ten events. By contrast, the Z-values for coupled EPSC charges obeyed a single normal distribution with a peak of  $Z \approx 2$  (Figure S4C;  $p = 0.094$ , Shapiro-Wilk test, and Pearson’s moment coefficient of skewness =  $-0.17$ ). We concluded that spines were classified into two distinct types: spines coupled with and spines coupled without

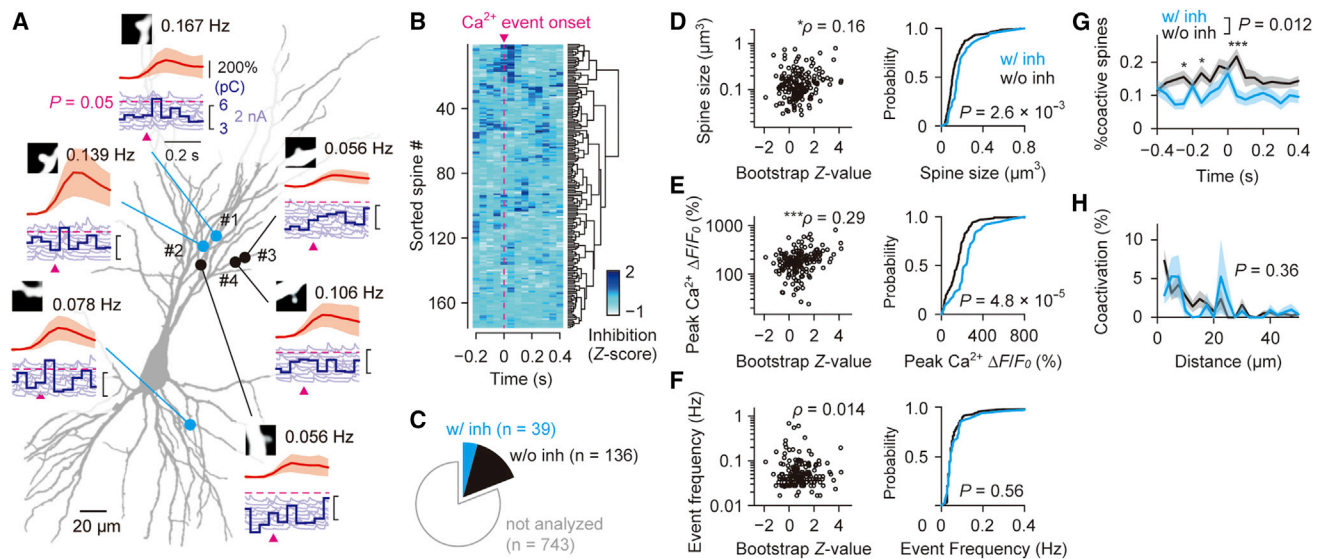


**Figure 3. Heterogeneous E/I Balances at Single Synapses**

(A) Morphology and activity of six example spines in three different videos taken from a single CA3 pyramidal cell are shown. The mean  $\pm$  SD traces of the calcium responses (red) and the mean inhibitory charge transfers (blue thick lines) were superimposed onto individual IPSC traces and aligned to the onsets of the individual calcium transients (arrowheads). The pink broken lines show the confidence levels of  $p = 0.05$  that were estimated from 100,000 resampled data points (Figure S4A). The blue-colored spines emitted calcium transients simultaneously with somatic IPSCs. The numbers beside the confocal images indicate the mean frequencies of the calcium transients in the spines.

(B) Normalized inhibitory charge transfers for 175 active spines were sorted along the Ward's dendrogram (right).

(C) Frequencies of the active spines whose calcium transients occurred with somatic inhibition (w/inh., blue) or without somatic inhibition (w/o inh., black) and the inactive spines (white).

(D–F) Spine head sizes (D), mean peak amplitudes of calcium transients (E), and calcium event frequencies (F) were plotted against the bootstrap-estimated Z-values of the level of inhibition coupled with the spines (left). The spine sizes and the peak calcium amplitudes were significantly correlated with the levels of somatic inhibition (Spearman's  $\rho = 0.16$ ,  $p = 0.037$  and  $\rho = 0.29$ ,  $p = 8.9 \times 10^{-5}$ , respectively), but not with the event frequencies ( $\rho = 0.014$  and  $p = 0.85$ ). The cumulative distributions of the spine sizes (D), the peak calcium amplitudes (E), and the event frequencies (F) in spines with (blue) and without (black) significant inhibition are shown (right). The p values were determined using the Mann-Whitney U test.

(G) Peri-spine activity time histogram of the total spine activity relative to the activity of the spines with and without inhibition. The data are shown as the means  $\pm$  SEMs ( $*p < 0.05$ ,  $***p < 0.001$ , and Tukey's test after two-way repeated-measures ANOVA).

(H) The mean  $\pm$  SEM probabilities of observing spines that were co-activated with a given spine are plotted as a function of the distance from the focused spine ( $p = 0.36$  and two-way repeated-measures ANOVA).

inhibition. In 39 of the 175 spines (22.3%), the activity was statistically judged to be followed by a significant increase in somatic inhibition (Figure 3C). We did not observe a specific pattern for the spatial distribution of inhibition-coupled spines over the dendritic trees because the path distances along the dendrites from the somata to these spines did not differ from the path distances to the spines without inhibition (Figure S4D;  $p = 0.27$ ,  $t_{10} = 1.17$ , and paired t test), and there was no difference between the probability that the spine nearest to an inhibition-coupled spine would be coupled to inhibition and the probability that the nearest neighbor of a spine without inhibition would be coupled with inhibition (Figure S4E;  $p = 0.070$ ,  $t_{10} = 2.03$ , and paired t test).

### Impact of Inhibition-Coupled Synapses

We observed that the mean amplitude for inhibition that was coupled with the activity of a given spine was positively correlated with both the head size of the spine (Figure 3D, left; Spearman's  $\rho = 0.16$ ,  $p = 0.037$ ) and the mean amplitude of the calcium transients that were evoked in the spine (Figure 3E, left;  $\rho = 0.29$ ,  $p = 8.9 \times 10^{-5}$ ), but not with the event frequency of the transients (Figure 3F, left;  $\rho = 0.014$ ,  $p = 0.85$ ). We also compared these pa-

rameters between two spine populations, spines with and spines without significant inhibition, and we obtained similar results: inhibition-coupled spines had larger spine heads (Figure 3D, right;  $p = 2.6 \times 10^{-3}$ ,  $Z = 3.02$ , and Mann-Whitney U test) and exhibited larger calcium transients (Figure 3E, right;  $p = 4.8 \times 10^{-5}$ ,  $Z = 4.07$ ) than spines without inhibition. The head sizes of spines are known to positively correlate with synaptic strength (i.e., the number of surface AMPA receptors) (Matsuzaki et al., 2001). Thus, our results suggest that the activation of spines that induce stronger excitation is accompanied by stronger global inhibition, which contributes to the E/I balance in local synaptic excitability in the neuron. The event frequencies of calcium transients did not differ between the inhibition-coupled and uncoupled spines (Figure 3F, right;  $p = 0.56$ ,  $Z = 0.58$ , and Mann-Whitney U test).

For spines with and without inhibition, we have separately illustrated the peri-activity time histograms showing the proportion of the total active spines. In these histograms, the percentage of spines that were co-activated with a given spine is plotted as a function of the time lag that followed the onset of activity of that spine (Figure 3G). The time histograms show peaks at

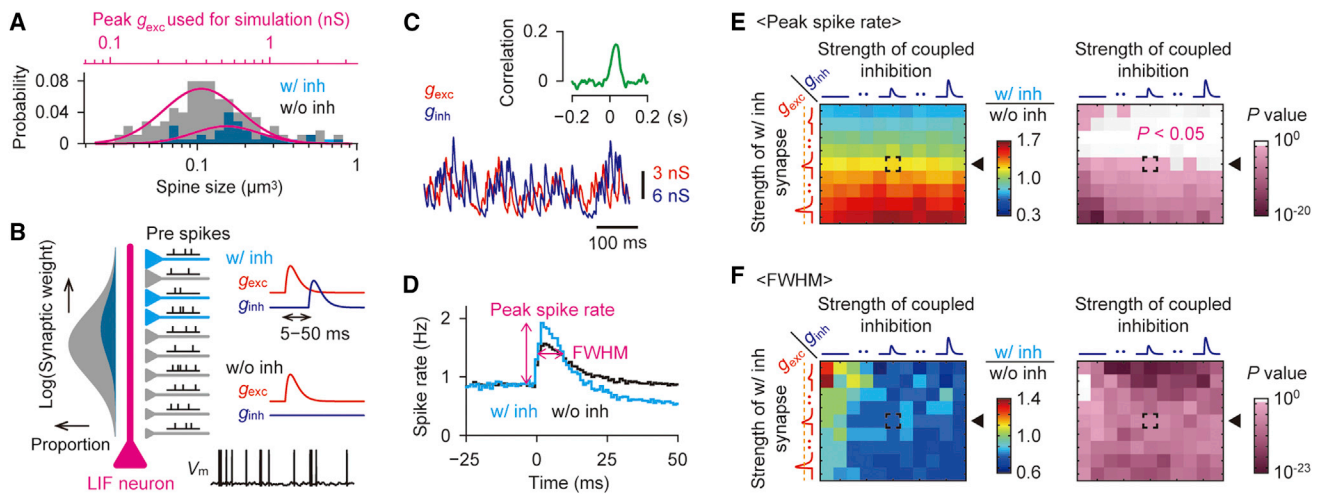


**Figure 4. Impact of Inhibition-Coupled Synapses on Postsynaptic Spikes: Numerical Simulation**

(A) The distribution of excitatory synaptic conductances ( $g_{exc}$ , simulation) was fitted to the lognormal distribution of the head sizes of the imaged spines (real data). The estimated conductances were centered at 0.53 nS (inhibition-coupled spines, blue) and 0.38 nS (other active spines, gray).  
 (B) Schematic of the simulation. A LIF neuron received excitatory inputs from 500 presynaptic neurons. Here, 20% of the synapses (100 out of 500) were set to “synapses with inhibition” (w/inh.), the activation of which was accompanied by a transient inhibitory conductance (5 nS) with a delay of 5–50 ms (blue). The synaptic conductances at an individual synapse were randomly sampled from the lognormal distributions of the synaptic conductances estimated in (A). Each synapse was activated as a pseudo-Poissonian unit at 1 Hz, and the firing behavior of the postsynaptic neuron was measured.  
 (C) Simulated excitatory and inhibitory synaptic conductances (red and blue, respectively). A cross-correlogram between the total of the excitatory and inhibitory conductances that occurred in the postsynaptic neuron is shown (inset).  
 (D) Mean probability of an action potential firing in the postsynaptic neuron relative to the timing of the activation of the inhibition-coupled synapses ( $n = 100$  synapses, blue) and other synapses ( $n = 400$  synapses, black).  
 (E and F) Impact of the strength of inhibition-coupled synapses and the subsequent inhibition on the spiking behavior of the LIF neuron. The average peak firing rate (E) and full width at half maximum (FWHM) of the response (F) that were evoked by inhibition-coupled synapses compared with those evoked by uncoupled synapses ( $n = 40$  LIF neurons) (left). Across the rows of the color map, the average excitatory conductance of the inhibition-coupled synapses ( $g_{exc}$ ) was systematically modified from 0.28 to 0.89 nS, whereas the average conductance of the uncoupled synapse was maintained at the same level (orange dots). The black arrowhead indicates the excitatory conductance that was used for the simulation in (B)–(D). Across the columns, the conductance of coupled inhibition ( $g_{inh}$ ) was modified from 0 to 10 nS. The boxed pixel in the color map corresponds to the results shown in (D). The statistical significance was evaluated using Student’s *t* tests (right). The significant pixels ( $p < 0.05$ ) were shaded in pink.

approximately 0–50 ms, indicating that the spines tended to be activated synchronously. Interestingly, although the peaks did not differ in their amplitudes, they appeared at 0 ms for the inhibition-coupled spines and at 50 ms for the spines without inhibition, suggesting a trend toward sequential activation starting with the spines without inhibition and followed by the inhibition-coupled spines. We previously reported that nearby spines are often synchronized (Takahashi et al., 2012). This tendency did not differ between the spines with and without inhibition (Figure 3H).

Inhibitory inputs can reset the accumulation of excitatory postsynaptic potentials, and somatic inhibition following spine activation may therefore enhance the temporal precision of action potential outputs (Pouille and Scanziani, 2001; Wehr and Zador, 2003). We confirmed this hypothesis using a simple computational model. We designed a leaky integrate-and-fire (LIF) neuron that received 500 excitatory synaptic inputs, including 100 synapses (20%) that were coupled with delayed inhibition. The synaptic strengths conformed to the distributions that were estimated from the head sizes of spines with and without inhibition (Figures 4A and 4B). Numerical simulation revealed that when synapses were activated in a pseudo-Poissonian fashion (Figure 4C), the activation of inhibition-coupled synapses more reli-

ably evoked action potentials in the LIF neuron than the activation of synapses without inhibition (Figures 4D and 4E). Moreover, as expected, the inhibition-coupled synapses more accurately elicited spikes within a narrow time window (Figures 4D and 4F). These results suggest a microscopic E/I-balancing mechanism in which the inhibitory microcircuitry provides selected excitatory pathways with “private” inhibition to improve the fidelity of spike transmission.

## DISCUSSION

In the present work, we discovered that synaptic excitation in dendritic domains that were  $>50 \mu\text{m}$  in length, which were found to contain 30–40 spines, was balanced by global inhibition recorded from the soma. Among these spines, 1–2 spines are expected to be coupled with inhibition because we found that of 175 active spines (out of a total of 918 spines, 19%), 22% were coupled with inhibition. Therefore, the subcellular E/I balance depends on a surprisingly small number of “balanced” spines. Consistent with this hypothesis, the E/I balance was found to be heterogeneous when dendrites were segmented into domains smaller than  $50 \mu\text{m}$ . Indeed, this heterogeneity was highlighted at individual spines, and this individual variety

across spines could work to differentially modulate inputs depending on their presynaptic origins.

The peaks of E/I correlation were offset toward delayed inhibition, with a lag of 0–50 ms. These results indicate that an IPSC arrives before an excitatory postsynaptic potential (EPSP) terminates. Therefore, IPSCs can trim the tails of EPSPs to sharpen their potential waveforms. Because inhibition-coupled spines had larger spine heads, inhibition may reduce the effective time windows of the synaptic inputs that can potentially strongly excite membrane potentials, which are therefore more likely to cause the initiation of action potentials. This mechanism may lead to more accurate action potential outputs. We speculate that accurate spike chains, induced via inhibition-coupled synapses or dendritic segments, serve as a functional packet to mediate the stable propagation of neural information. Functional compartmentalization is the key to dendritic computation and can include local dendritic electrogenesis, synaptic plasticity, or synchronized inputs (Goldberg and Yuste, 2005; Häusser et al., 2000). Therefore, the E/I equilibrium that we describe here may cooperate with these functions to contribute to the somatic readout of dendritic computations.

The recorded neurons were voltage-clamped and thus could not fire action potentials. This configuration excludes the involvement of feedback inhibition triggered by the recorded cells. Therefore, the coupled inhibition is likely to arise from lateral feedback inhibition via other neurons or from feedforward inhibition recruited by upstream network activity. Recent studies have identified a circuit mechanism that can equalize the E/I balance in the mouse visual cortex and hippocampus. In this mechanism, pyramidal cells receive somatic inhibition from parvalbumin-positive interneurons that is in proportion to their excitation level (Mizunuma et al., 2014; Xue et al., 2014). Identifying the type of interneuron that is responsible for this phenomenon will reveal the source of the somatic inhibition that occurs after the activation of specific spines.

In our experimental configurations, IPSCs contributed more than 86% of the total PSCs. Although we regarded outward synaptic currents as IPSCs, the remaining inward currents (EPSCs) might have counteracted the IPSCs to some extent, resulting in false-negative detections of inhibition-coupled spines. This contamination could therefore underestimate the ratio of inhibition-coupled spines (herein, estimated to be 22%). Moreover, inhibition tended to be coupled with larger spines and was more likely to be masked by their own EPSCs, because larger spines evoke larger EPSCs (Matsuzaki et al., 2001). As a result, the actual correlation between the spine size and the amplitude of the coupled inhibition may be stronger than we measured here. Finally, we obtained data exclusively from slice cultures because we were unable to conduct the same experiments using acute slice preparations. Spontaneous activity is very sparse in acute slices, and their less transparent tissues hindered our ability to perform large-scale, high-speed optical imaging of spine calcium. Although the microcircuits in slice cultures may be reorganized to some extent, it is worth noting that cultured networks have been shown to emit more *in vivo*-like spontaneous activity than acute slices (Okamoto et al., 2014; Takahashi et al., 2010, 2012).

## EXPERIMENTAL PROCEDURES

### Animals

Experiments were performed with the approval of the animal experiment ethics committee at the University of Tokyo (approval number: 19-43) according to the University of Tokyo guidelines for the care and use of laboratory animals. Unless otherwise specified, all averaged values are reported as the means  $\pm$  SDs.

### Slice Culture Preparation

Hippocampal organotypic slices were prepared from 7-day-old Wistar/ST rats. Rat pups were anesthetized using hypothermia and decapitated. Brains were cut into 300- $\mu$ m-thick slices in ice-cold Grey's balanced salt solution supplemented with 25 mM glucose. The slices were placed on Omnipore membrane filters and incubated in 5% CO<sub>2</sub> at 37°C. The culture medium (50% minimal essential medium, 25% Hank's balanced salt solution, 25% horse serum, and antibiotics) was changed every 3.5 days. Experiments were performed between 12 and 19 days *in vitro*.

### Electrophysiology and Imaging

Organotypic slices were transferred to a recording chamber (30–32°C) perfused with artificial cerebrospinal fluid (aCSF) (127 mM NaCl, 26 mM NaHCO<sub>3</sub>, 3.5 mM KCl, 1.24 mM KH<sub>2</sub>PO<sub>4</sub>, 1.0 mM MgSO<sub>4</sub>, 1.8–2.4 mM CaCl<sub>2</sub>, 10 mM glucose, and 200  $\mu$ M Tetrox). Whole-cell recordings were made from CA3 pyramidal cells using a MultiClamp 700B amplifier (Molecular Devices). Patch pipettes (4–6 M $\Omega$ ) were filled with 130 mM CsMeSO<sub>4</sub>, 10 mM CsCl, 10 mM HEPES, 10 mM phosphocreatine, 4 mM MgATP, 0.3 mM NaGTP, 0.2% biocytin, and 200  $\mu$ M Fluo-5F. During the recordings, the cells were voltage-clamped at –30 mV to amplify inhibition-driven outward currents (i.e., IPSCs) in cell bodies and receptor-mediated calcium currents in dendritic spines. In some experiments, we used an intracellular solution with a higher Cl<sup>–</sup> concentration (92 mM CsCl) to voltage-clamp the cells at close to the IPSC reversal potential and, in these cells, we primarily recorded excitation-driven inward currents (i.e., EPSCs). Images were acquired at 20 frames/s using a Nipkow-disk confocal unit (Yokogawa Electric), a cooled electron multiplying charge-coupled device (EM-CCD) camera (Andor), and a water-immersion objective lens (40 $\times$ , 0.80 NA). Fluorophores were excited using a 488-nm laser (0.8 mW) and visualized using a 507-nm long-pass emission filter. To minimize the space-clamp effect, only spines located within 200  $\mu$ m from the soma were imaged in the CA3 stratum oriens and stratum radiatum.

### Imaging Analysis

For each spine, the calcium fluorescence change  $\Delta F/F_0$  was calculated as  $(F_t - F_0)/F_0$ , where  $F_t$  is the fluorescence intensity at frame time  $t$  and  $F_0$  is the baseline. For spine size estimations, we first calculated the area of the cross-section in a hand-traced image of the spine. By assuming that the spine heads were spherical, we approximated the radius of the sphere from the cross-section area, and we then estimated the spine size as the volume of the sphere.

All analyses were performed using ImageJ and custom scripts written in MATLAB.

### Simulation

We modeled a conductance-based LIF neuron using the following equation:

$$\tau_m \frac{dV}{dt} = V_{rest} - V + g_{exc}(t)(E_{exc} - V) + g_{inh}(t)(E_{inh} - V),$$

where  $\tau_m = 20$  ms,  $V_{rest} = -70$  mV,  $E_{exc} = 0$  mV, and  $E_{inh} = -70$  mV. The functions  $g_{exc}(t)$  and  $g_{inh}(t)$  represent the excitatory and inhibitory synaptic conductances, respectively. When the membrane potential  $V$  reached a spike threshold of –50 mV, the neuron fired an action potential and the membrane potential then reset to –65 mV. The neuron had 500 excitatory synapses, each of which was randomly and independently activated at 1 Hz. Twenty percent of the excitatory synapses were set to be inhibition-coupled synapses. Activation of the inhibition-coupled synapses was accompanied by inhibitory conductances of 5 nS and with delays that varied randomly from 5 to 50 ms

in each trial. The peak conductance of each excitatory synapse was obtained from an estimated conductance distribution that was based on observations of spine size frequency and it ranged from 0.1 to 3.7 nS (Figure 4A). In addition to inhibitions that counteracted these excitatory synaptic inputs, the neuron also received inhibitory inputs (1 nS) that fired randomly at 100 Hz. Both the excitatory and the inhibitory synaptic conductances were modeled by a dual exponential function,  $g_0(e^{-t/\tau_1} - e^{-t/\tau_2})$  using a scaling factor,  $g_0$ , and the time constants  $\tau_1 = 1$  ms and  $\tau_2 = 8$  ms. We simulated the membrane potential of the neuron for 300 s at a time step of 1 ms. In some simulations, we systematically modified the excitatory conductance of inhibition-coupled synapses and the conductance of coupled inhibition. For each condition, we generated 40 LIF neurons with different sets of synapses and simulated their firing behavior to obtain an average spiking response and to conduct a statistical evaluation (Figures 4E and 4F).

### SUPPLEMENTAL INFORMATION

Supplemental Information includes four figures and can be found with this article online at <http://dx.doi.org/10.1016/j.celrep.2016.01.024>.

### AUTHOR CONTRIBUTIONS

N.T. and Y.I. designed the study. N.T., C.K., and T.I. conducted the experiments. N.T. analyzed the data. N.T. and Y.I. wrote the paper.

### ACKNOWLEDGMENTS

This work was partially supported by Grants-in-Aid for Science Research from the Ministry of Education, Culture, Sports, Science, and Technology of Japan (nos. 22115003 and 25119004).

Received: July 30, 2015

Revised: November 19, 2015

Accepted: January 4, 2016

Published: February 4, 2016

### REFERENCES

Anderson, J.S., Carandini, M., and Ferster, D. (2000). Orientation tuning of input conductance, excitation, and inhibition in cat primary visual cortex. *J. Neurophysiol.* *84*, 909–926.

Cafaro, J., and Rieke, F. (2010). Noise correlations improve response fidelity and stimulus encoding. *Nature* *468*, 964–967.

Chen, X., Leischner, U., Rochefort, N.L., Nelken, I., and Konnerth, A. (2011). Functional mapping of single spines in cortical neurons in vivo. *Nature* *475*, 501–505.

Chen, T.W., Wardill, T.J., Sun, Y., Pulver, S.R., Renninger, S.L., Baohan, A., Schreiter, E.R., Kerr, R.A., Orger, M.B., Jayaraman, V., et al. (2013). Ultrasensitive fluorescent proteins for imaging neuronal activity. *Nature* *499*, 295–300.

Froemke, R.C. (2015). Plasticity of cortical excitatory-inhibitory balance. *Annu. Rev. Neurosci.* *38*, 195–219.

Goldberg, J.H., and Yuste, R. (2005). Space matters: local and global dendritic Ca<sup>2+</sup> compartmentalization in cortical interneurons. *Trends Neurosci.* *28*, 158–167.

Häusser, M., Spruston, N., and Stuart, G.J. (2000). Diversity and dynamics of dendritic signaling. *Science* *290*, 739–744.

Isaacson, J.S., and Scanziani, M. (2011). How inhibition shapes cortical activity. *Neuron* *72*, 231–243.

Liu, G. (2004). Local structural balance and functional interaction of excitatory and inhibitory synapses in hippocampal dendrites. *Nat. Neurosci.* *7*, 373–379.

Matsuzaki, M., Ellis-Davies, G.C., Nemoto, T., Miyashita, Y., Iino, M., and Katsai, H. (2001). Dendritic spine geometry is critical for AMPA receptor expression in hippocampal CA1 pyramidal neurons. *Nat. Neurosci.* *4*, 1086–1092.

Mizunuma, M., Norimoto, H., Tao, K., Egawa, T., Hanaoka, K., Sakaguchi, T., Hioki, H., Kaneko, T., Yamaguchi, S., Nagano, T., et al. (2014). Unbalanced excitability underlies offline reactivation of behaviorally activated neurons. *Nat. Neurosci.* *17*, 503–505.

Okamoto, K., Ishikawa, T., Abe, R., Ishikawa, D., Kobayashi, C., Mizunuma, M., Norimoto, H., Matsuki, N., and Ikegaya, Y. (2014). Ex vivo cultured neuronal networks emit in vivo-like spontaneous activity. *J. Physiol. Sci.* *64*, 421–431.

Okun, M., and Lampl, I. (2008). Instantaneous correlation of excitation and inhibition during ongoing and sensory-evoked activities. *Nat. Neurosci.* *11*, 535–537.

Pouille, F., and Scanziani, M. (2001). Enforcement of temporal fidelity in pyramidal cells by somatic feed-forward inhibition. *Science* *293*, 1159–1163.

Takahashi, N., Sasaki, T., Matsumoto, W., Matsuki, N., and Ikegaya, Y. (2010). Circuit topology for synchronizing neurons in spontaneously active networks. *Proc. Natl. Acad. Sci. USA* *107*, 10244–10249.

Takahashi, N., Kitamura, K., Matsuo, N., Mayford, M., Kano, M., Matsuki, N., and Ikegaya, Y. (2012). Locally synchronized synaptic inputs. *Science* *335*, 353–356.

Wehr, M., and Zador, A.M. (2003). Balanced inhibition underlies tuning and sharpens spike timing in auditory cortex. *Nature* *426*, 442–446.

Xue, M., Atallah, B.V., and Scanziani, M. (2014). Equalizing excitation-inhibition ratios across visual cortical neurons. *Nature* *511*, 596–600.

Yuste, R., and Denk, W. (1995). Dendritic spines as basic functional units of neuronal integration. *Nature* *375*, 682–684.

**Cell Reports, Volume 14**

**Supplemental Information**

**Subcellular Imbalances in Synaptic Activity**

**Naoya Takahashi, Chiaki Kobayashi, Tomoe Ishikawa, and Yuji Ikegaya**

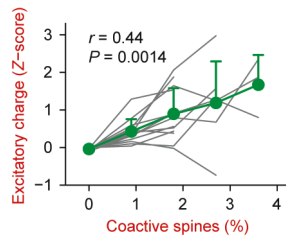


**Figure S1. Correlation between imaged synaptic activity and global excitation. Related to Figure 1.**

Relationship between the summed spine activity in a given video frame and the excitatory charge transfer recorded from the soma is described. EPSCs were recorded from cells clamped at a voltage close to the reversal potential of IPSCs using a high  $\text{Cl}^-$  intracellular solution (see Experimental procedures). The green line represents the means  $\pm$  SDs of 13 videos recorded for 13 cells (gray lines). Synaptic excitation in imaged dendrites and global excitatory inputs were significantly correlated (Pearson's  $r = 0.44$ ,  $P = 1.4 \times 10^{-3}$ ).

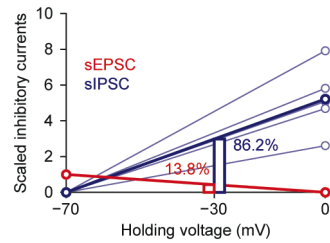


**Figure S2. Excitatory and inhibitory components in recorded synaptic currents. Related to Figure 1.**

Spontaneous excitatory and inhibitory synaptic currents were separately recorded at holding voltages of  $-70$  mV and  $0$  mV, which corresponded to the reversal potentials of IPSCs and EPSCs, respectively. The mean IPSCs were normalized by the mean EPSCs. The current-*versus*-voltage relationship indicates that IPSCs accounted for  $86.2 \pm 5.1\%$  of the total PSCs at  $-30$  mV ( $n = 5$  cells).

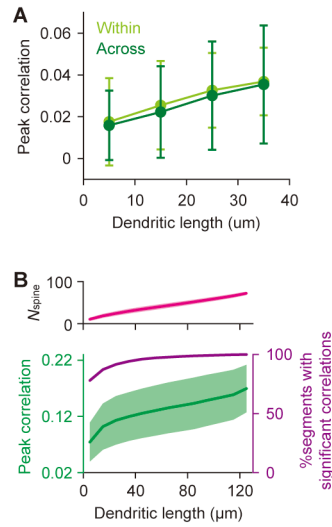


**Figure S3. Synaptic balance in dendritic segments. Related to Figure 2.**

(A) E/I correlations within and across dendritic branches. Peak E/I correlation values are compared between dendritic segments collected from the same dendritic branches (light green) and those collected from different branches (dark green). The data represent the means  $\pm$  SDs of 1,351 branches (within) and 3,415 branches (across).

(B) Correlation between spine activity and global excitation in local dendritic segments. Bottom: The peak correlation between spine activity and global excitation as a function of the lengths of the dendritic segments generated from different sets of dendritic parts in a single cell (mean  $\pm$  SD, green,  $n = 2,560$  segments). The ratio of dendritic segments with significant correlation peaks to the total number of segments tested is superimposed (purple). Top: The numbers of spines involved in the summed segments (mean  $\pm$  SD, pink).

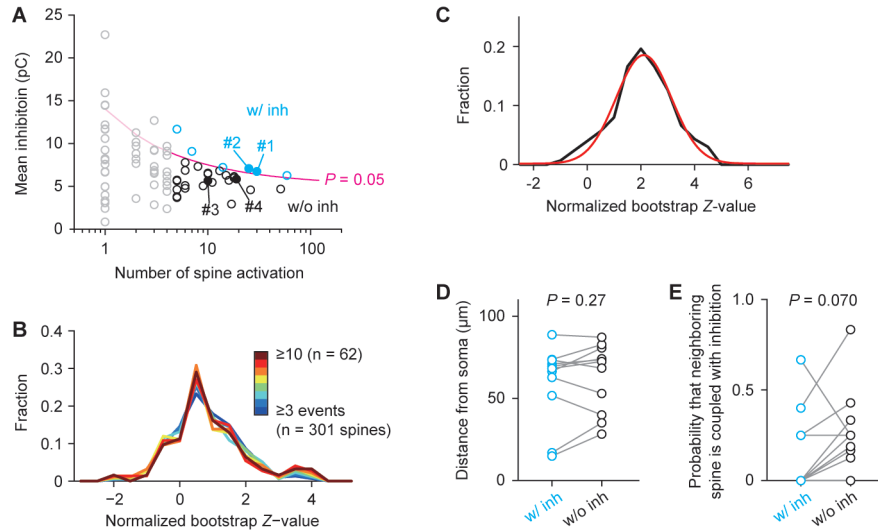


**Figure S4. Statistical evaluation of global inhibition coupled to spine activity. Related to Figure 3.**

(A) The relationship between the number of calcium transients emitted by individual spines during the observation time and the peak amplitudes of the mean inhibitory charge transfers within two frames (0 and 50 ms) after spine activity. Each circle indicates a single spine. To determine whether significant inhibition followed the activity of a spine, we estimated the probability of fluctuations occurring in the inhibitory charge transfers using randomly resampled data. When a spine was activated  $N$  times during the observation period, each resample consisted of the average number of inhibitory charge transfers in  $N$  time epochs (50 ms), which was randomly chosen from the entire whole-cell recording trace. For each spine, the chance was computed based on 100,000 resampled surrogates. Spines with activity that was followed by inhibition that was larger than the probability, within the delays of 50 ms ( $P = 0.05$ , pink line), were defined as inhibition-coupled spines (w/ inh., blue). To avoid statistical errors, we analyzed only the spines that were activated more than four times during the observation period (blue and black). The circles with numbers (#1–4) correspond to the spines shown in Figure 3A.

(B) Distribution of bootstrap-estimated Z-values for the levels of inhibition that were coupled to active spines. Colored lines correspond to different thresholds of the number of calcium events during the observation period. Regardless of the number of events, the Z-values

showed a positively skewed distribution with a tail at high Z-values.

(C) Distribution of bootstrap-estimated Z-values for global excitation coupled to active spines that showed  $\geq 5$  calcium events during the observation period (black line,  $n = 301$  spines). Probability of the Z-values showed a normal distribution (fitted by the red line,  $P = 0.094$ , Shapiro-Wilk test; Pearson's moment coefficient of skewness =  $-0.17$ ).

(D) The path distance from the soma did not differ between spines with and without inhibition.  $P = 0.27$ ,  $t_{10} = 1.17$ , paired  $t$ -test ( $n = 11$  videos).

(E) The probability that the spine nearest to a given spine would be coupled with inhibition differed between inhibition-coupled and uncoupled spines.  $P = 0.070$ ,  $t_{10} = 2.03$ , paired  $t$ -test ( $n = 11$  videos). Note that the only video that contained no inhibition-coupled spines was not analyzed.